JACS
JOURNAL OF THE AMERICAN CHEMICAL SOCIETY

Article

pubs.acs.org/JACS

Multi-Stimuli-Responsive Charge-Transfer Hydrogel for Room-Temperature Organic Ferroelectric Thin-Film Devices

Makam Pandeeswar,[†] Satyaprasad P. Senanayak,[‡] K. S. Narayan,*[,‡] and T. Govindaraju*[,†]

[†]Bioorganic Chemistry Laboratory, New Chemistry Unit, and [‡]Molecular Electronics Lab, Chemistry and Physics of Materials Unit, Jawaharlal Nehru Centre for Advanced Scientific Research, Jakkur P.O., Bengaluru 560064, India

Supporting Information

ABSTRACT: The possibility of designing programmable thin-film supramolecular structures with spontaneous polarization widens the utility of facile supramolecular chemistry. Although a range of low molecular mass molecular single crystals has been shown to exhibit ferroelectric polarization, demonstration of stimuli-responsive, thin-film, solution-processable supramolecular ferroelectric materials is rare. We introduce aromatic π-electron donor−acceptor molecular systems responsive to multiple stimuli that undergo supramolecular chiral mixed-stack charge-transfer (CT) coassembly through the tweezer-inclusion-sandwich process supported by hydrogen-bonding interactions. The structural synergy originating from hydrogen-bonding and chiral CT interactions resulted in the development of spontaneous unidirectional macroscopic polarization in the crystalline nanofibrous hydrogel network, under ambient conditions. Moreover, the tunability of these interactions with optical, mechanical, thermal, and electrical stimuli allowed the design of multistate thin-film memory devices. Our design strategy of the supramolecular motif is expected to help the development of new molecular engineering strategies for designing potentially useful smart multicomponent organic electronics.

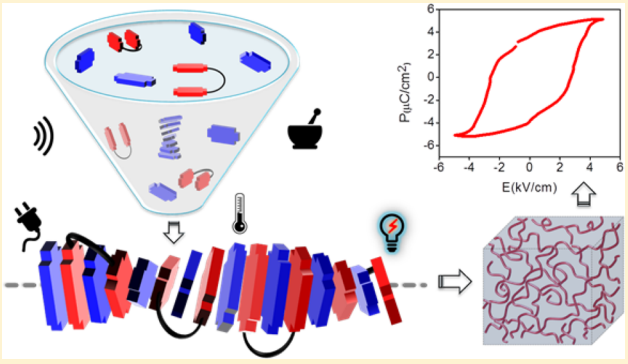

INTRODUCTION

Development of smart multifunctional organic nanomaterials with optical and electroactive properties is of special interest for new-generation optoelectronic applications, owing to the advantage of solution processability.[1−9] One of the interesting and rarely observed properties in organic materials is ferroelectricity (FE). Ferroelectric materials enable the switching of electric dipoles, which find a wide range of applications in sensors, actuators, energy-efficient memory units, and photonics.[10−14] Unlike their inorganic counterparts, the organic ferroelectric (OFE) phenomenon is observed in limited material systems and is typically accompanied by sizable coercive field.[15] Hence, an alternative approach to developing low coercive field organic ferroelectrics based on the supramolecular assembly of appropriately designed multicomponent molecular systems is quite promising.[10,11,16−18] Induction of the ferroelectric property in low molecular mass organic compounds can be done through the introduction of ordered dipoles by weak noncovalent interactions like hydrogen bonding and charge-transfer (CT) interactions or by encapsulation of dipoles in three-dimensional (3D) lattice or metal−organic frameworks (MOF).[10,19,20] The pioneering work of Tokura and co-workers demonstrated multicomponent OFE molecular solids, wherein the ferroelectric polarization switching arises from molecular displacement or collective transfer of electrons or protons.[10,21] On the other hand, recent investigations regarding supramolecular π-electron donor−acceptor mixed-stack CT networks have displayed promising ferroelectric properties due to their long-range unidirectional orientation of CT dipoles.[19,22] However, the ferroelectric switching property of the known OFE−CT superstructures prevails only at low temperatures (below 71 K).[23,24] Recently, Stupp and co-workers demonstrated room-temperature ferroelectricity in mixed-stack CT single crystals and attributed it to a combination of orthogonal noncovalent hydrogen bonding and CT interactions.[19,25] Notably, all the reported low molecular mass OFEs (hydrogen bonded, mixed-stack CT complexes, and a combination of both) exhibit ferroelectric polarization switching in their single crystalline solids.

The option of OFE without the single crystal requirements extends their utility to a larger range of applications encompassing flexible and printable electronic devices.[10,11,19] The presence of long-range order at room temperature and beyond, coupled with facile processing methods, opens up model systems that are of both fundamental and technological interest. In this line of pursuit, to demonstrate solution-processable, low molecular weight, room-temperature organic ferroelectrics, the two key challenges posed are (i) unidirectional non-centrosymmetric alignment of molecular electric dipoles and (ii) transfer of assemblies from the solution onto the substrate.

Received: April 30, 2016
Published: June 15, 2016

DOI: 10.1021/jacs.6b03811
J. Am. Chem. Soc. 2016, 138, 8259−8268

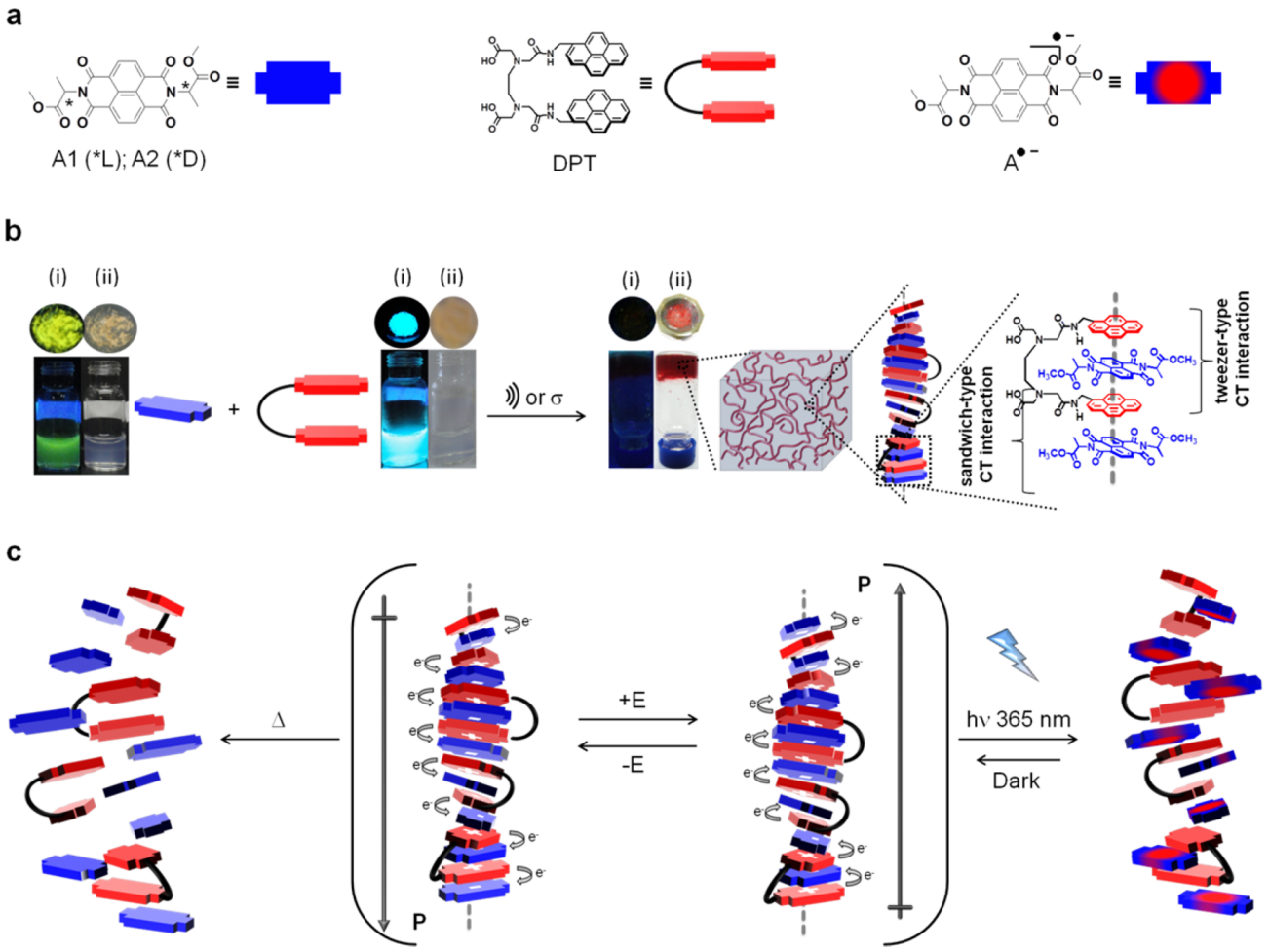

Figure 1. Molecular structures and schematic representation of multi-stimuli-responsive TIS−CT co-assembly of DPT and A1/A2. (a) Molecular structures and schematic representation of acceptors (A1, L-alanine methyl ester conjugated NDI; A2, D-alanine methyl ester conjugated NDI), donor (DPT), and $A^{\bullet -}$ radicals. (b) Photographs of aqueous solution/solids of A1, DPT, and mechanical-stimuli-induced {ultrasonication [))))] for solution and grinding (σ) for solid powders} A1+DPT TIS−CT co-assembled (A1:DPT 2:1) hydrogel (inverted vial) and solid powders under UV (i) and visible light (ii); schematic representation of corresponding P-type (right handed) self-assembly of A1 and TIS−CT co-assembly. (c) Schematic illustration of electric field (E) induced net polarization (P) switching, temperature (Δ) driven disassembly, and UV-irradiation ($h\nu$ 365 nm) responsive photoinduced single-electron transformation reaction within the TIS−CT co-assembly, respectively.

We present strategies implemented toward tackling these issues, by introducing chiral supramolecular hydrogels based on the structural synergy between hydrogen-bonding and mixed-stack CT-interaction-driven co-assembly, which facilitate a strong network of ordered dipoles and exhibit thin-film ferroelectricity at room temperature. In this approach, the CT-interaction-driven donor−acceptor dimerization breaks the center of symmetry of the superstructure lattice,[25,26] and induction of macroscopic supramolecular chirality harnesses the spontaneous polarization through conformational preference of transverse molecular dipoles to orient in a particular direction;[27−29] the inherent solidlike behavior of the CT hydrogel-based supramolecular polymeric network allows the transfer of the preformed assemblies onto substrates without the aid of any sophisticated instrumentation.[30,31] Furthermore, we demonstrate optically switchable, energy-efficient, multi-state, thin-film ferroelectric memory devices fabricated from these organic materials, which operate under ambient conditions. Moreover, we demonstrate that the generality of this design principle can lead to a new generation of smart materials with a wide range of functional applications.

RESULTS AND DISCUSSION

Two-component mixed-stack CT hydrogels are a special class of multicomponent systems, which are challenging to achieve because of commonly encountered problems such as self-sorting or phase separation.[32] Hence, careful designing of π-electron donor (D) and acceptor (A) molecular systems is crucial to achieving CT hydrogels with high-level molecular ordering in the form of extended D−A mixed stacks. In the present study, we designed an amphiphilic and flexible π-electron-rich dipyrene tweezer-like (DPT) molecular system (pyrene is π-basic with molecular quadrupole moment Q_{zz} = −13.8 B) suitable for complexing electron-deficient aromatic guest molecules such as naphthalenediimides (NDIs) (NDI is π-acidic with Q_{zz} = +18.6 B) by encapsulating them in the tweezer cavity (tweezer-inclusion complexation) as well as through intermolecular sandwiching of the tweezer-inclusion complexes (TIS: tweezer-inclusion sandwich) (Figure 1a,b).[33,34] The two carboxylic acid functionalities on the backbone of DPT were expected to impart aqueous solubility and lateral extension of assemblies through intermolecular hydrogen bonding. The alanine methyl ester-functionalized

DOI: 10.1021/jacs.6b03811
J. Am. Chem. Soc. 2016, 138, 8259−8268

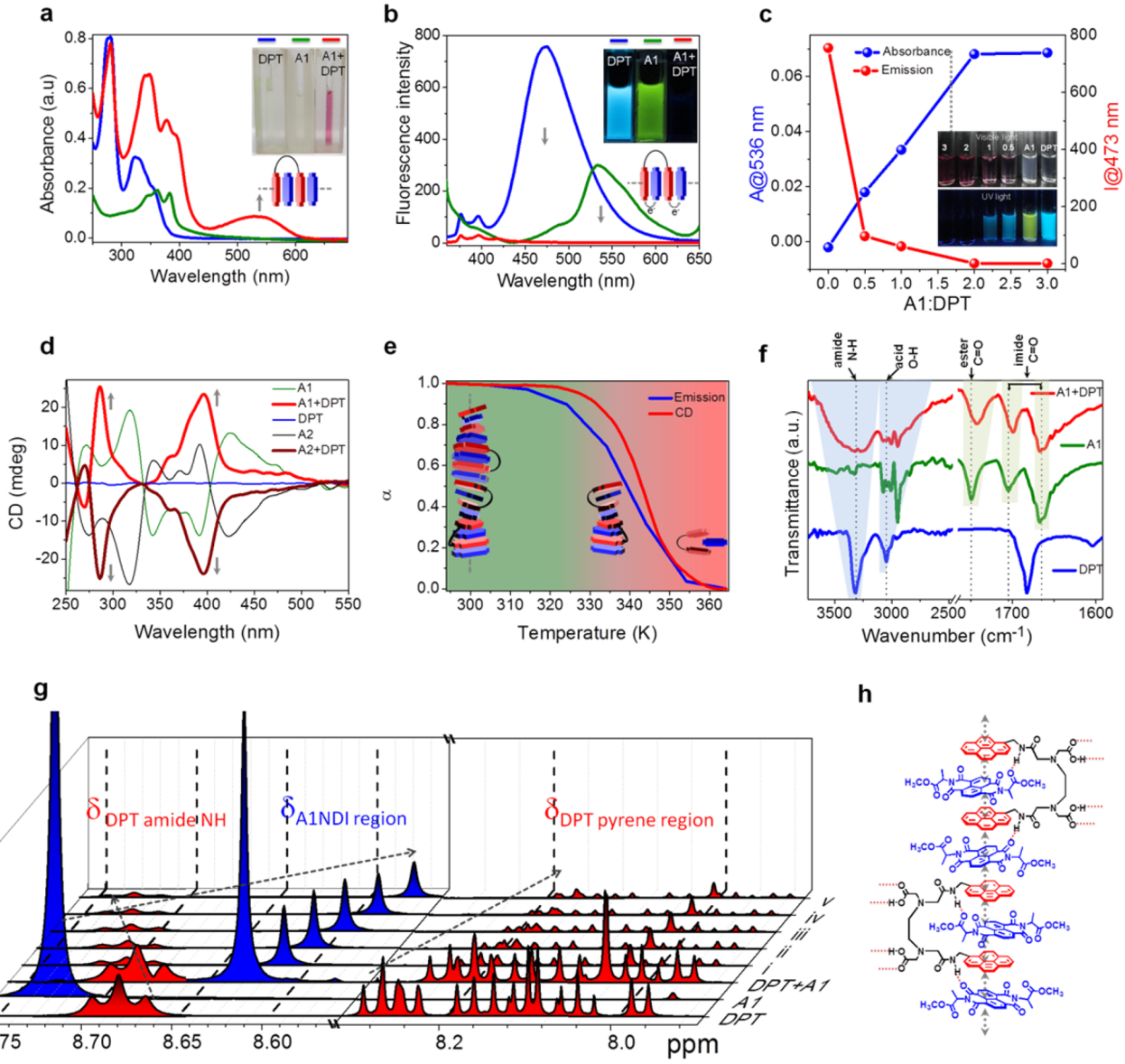

Figure 2. Spectroscopic characterization of TIS−CT co-assembly of DPT and A1/A2 in aqueous solution. (a) UV−vis absorption spectra and photographs of corresponding aqueous solutions under visible light; schematic representation of TIS−CT co-assembly. (b) Fluorescence emission spectra (excitation wavelength = 340 nm) and corresponding aqueous solution photographs under UV light; schematic representation of charge transfer (electron) within the TIS co-assembly. (c) Plot of CT absorption at 536 nm (blue line) and fluorescence excimer (FE) emission intensity at 475 nm (red line) as a function of the fraction of A1 added to DPT (A1/DPT = 0.5, 1, 2, and 3). Inset: photographs of corresponding aqueous solutions under visible and UV light show an increase in CT color (red) and gradual fluorescence quenching. (d) CD spectra of the mirror image chiral self-assemblies of A1 and TIS−CT coassemblies (A1/A2+ DPT), respectively. (e) The plot of the fraction of CT-TIS co-assembly aggregates (α) [derived from VT-FE and VT-CD at 475 nm (Blue line) and 400 nm (red line), respectively] as a function of temperature; schematic representation of thermal denaturation of chiral TIS−CT co-assembly. (f) ATIR spectra (3732−2463 and 1765−1592 cm^{-1} region) of fully dried aqueous solutions of DPT and A1 and xerogels of A1+DPT (2:1 A1:DPT). (g) ^{1}H NMR spectra of DPT amide region (8.76−8.66 ppm, red), A1 NDI aromatic ring region (8.75−8.55 ppm, blue), and DPT pyrene aromatic region (8.30−7.90 ppm) in DMSO-d_6 (400 μL) as a function of addition of water: (I) 4 μL, (II) 8 μL, (III) 16 μL, (IV) 20 μL, and (V) 24 μL. Dotted arrows indicate the chemical shifts upon addition of water. (h) Proposed molecular model for the formation of extended mixed-stack TIS−CT co-assembly between DPT and A1/A2 via complementary $\pi-\pi$ stacking and hydrogen-bonding interactions.

NDIs (A1 and A2) were designed as aromatic acceptor molecules to achieve chiral (noncentrosymmetric) supramolecular CT coassemblies through a TIS (Figure 1a,b).[35−39] The first indication of TIS−CT co-assembly by DPT and A1 came from the visible color and fluorescence change, as shown in Figure 1b [Movie 1, Supporting Information (SI)]. The aqueous solutions as well as solid powder forms of both individual DPT and A1/A2 were found to be colorless and highly fluorescent in nature. However, after mixing them together at 2:1 (A1:DPT), under external mechanical stimuli (grinding for solid samples and ultrasound for solutions), they turned into nonfluorescent and visibly red-colored powder and hydrogel, respectively. Therefore, it can be stated that the mechanical stimulus-induced formation of the TIS−CT co-assembly between DPT and A1 can be achieved in solution as well as in solvent-free solid state. The extensive spectroscopy

DOI: 10.1021/jacs.6b03811
J. Am. Chem. Soc. 2016, 138, 8259−8268

and microscopic studies indeed indicated the formation of chiral TIS−CT co-assembly upon mixing DPT and A1/A2 in 2:1 (A1/A2:DPT) ratio in both aqueous solutions (DMSO/water 20/80, v/v) and the solid state. Furthermore, the chiral TIS−CT co-assembly was found to be responsive toward external stimuli such as light and temperature, as shown in Figure 1c.

A detailed procedure for the synthesis and characterization of DPT and A1/A2 is provided in the Experimental Section. The formation of mixed-stack CT co-assembly was confirmed by recording the absorption spectrum of thoroughly mixed 2:1 A1:DPT aqueous solution (DMSO/water: 20/80, v/v) and coground solid powders [Figures 2a and S6 (SI)]. The appearance of a new broad absorption band in the visible region centered at 536 nm (λ_{max}), both in solution and ground powders, which was absent in the individual spectra of DPT and A1, was a characteristic feature of the mixed-stack CT interaction between DPT and A1.[40] In accordance with the UV−vis absorption data, the CT interaction between DPT and A1 was further evident from the fluorescence emission spectra of 2:1 A1:DPT aqueous solution and coground solid powder [Figures 2b and S6 (SI)]. The samples exhibited total fluorescence quenching of individual donor (DPT) and acceptor (A1) emission bands, suggesting the nonradiative charge (electron) transfer interactions between DPT and A1 within the TIS co-assembly, as shown in the inset of Figure 2b.

To determine the stoichiometry of A1 to DPT for the formation of efficient CT mixed-stack co-assembly, absorption and fluorescence emission spectra were recorded at different concentrations of A1 [$(1-4) \times 10^{-4}$ M] mixed with a fixed concentration of DPT (2×10^{-4} M). The inset in Figure 2c shows the photographs of corresponding solutions under visible as well as UV light. The plot of absorbance at the CT band (λ_{max} = 536 nm) and DPT excimer emission band (473 nm) versus the fraction of A1 added to DPT (A1:DPT) provided conclusive evidence for the 2:1 (A1:DPT) CT co-assembly. At this concentration ratio, maximum absorbance of the CT absorption band (λ_{max}= 536 nm) was observed, which also corresponds to complete fluorescence quenching of both DPT and A1. Notably, the formation of a 2:1 (A1:DPT) stoichiometric ratio also indicated the formation of DPT−A1−DPT−A1 (D−A−D−A) stacks with A1 molecules arranged inside the tweezer cavity of DPT as well as outside it, like a tweezer sandwich, to form an extended donor−acceptor TIS−CT co-assembly (Figure 1b).

To investigate the long-range intermolecular orientations within the mixed-stack CT co-assembly, circular dichroism (CD) spectra was recorded in aqueous solution. The individual enantiomerically pure acceptors A1 and A2 displayed mirror image positive and negative Cotton effects with λ_{max} at 422 nm, suggesting the formation of right-handed (*P*-type) and left-handed (*M*-type) chiral self-assemblies, respectively. Contrastingly, the achiral DPT showed a flat CD signal, indicating the absence of any preferential helical organization. Under similar conditions, the CT co-assembly of DPT:A1/A2 (1:2) displayed strong induced CD (ICD) signals at both pyrene (λ_{max} = 285 nm) and NDI (λ_{max}= 406 nm) absorption regions, with bands similar to that of individual chiral self-assembly of the acceptor (A1/A2). This suggested the acceptor (A1/A2)-induced chiral heterochromophoric exciton coupling between pyrene (DPT) and NDI (A1/A2) chromophores within the CT co-assembly (Figures 2d and 1b).

To assess the thermal stability of A1/A2+DPT (A1:DPT 2:1) CT co-assembly, variable-temperature-dependent absorption measurements were carried out. An increase in the temperature from 288 to 368 K significantly modified the UV−vis spectra (Figure S7, SI). A reduction in the intensity of the CT band at 536 nm and aggregation band at 400 nm was observed with the restoration of vibronically structured monomeric absorption bands of pyrene and NDI at 250 and 380 nm, respectively. We further examined the variable-temperature-dependent fluorescence emission and CD behavior of the A1+DPT CT co-assembly. As the temperature increased from 293 to 368 K, a strong enhancement (∼2 orders of magnitude) in DPT excimer emission (at λ_{max} = 475 nm) was observed (Figure S7, SI). In contrast, variable-temperature CD experiments (293−343 K) exhibited a decrease in ICD intensity at both DPT (λ_{max} = 285 nm) and A1/A2 aggregation (λ_{max} = 400 nm) bands (Figure S7, SI). These features are evident from the plot of the fraction of aggregates (α) versus temperature (293−363 K), as shown in Figure 2e. The nonemissive and intense ICD signals (α = 1) at the low-temperature region (293−324 K) revealed the existence of a nonfluorescent right-handed TIS−CT mixed-stack co-assembly. However, a further increase in temperature (324−368 K) resulted in strong enhancement of the fluorescence intensity, followed by a decrease of ICD signals (α = 0), suggesting the thermally induced release of acceptor molecules (A1) from TIS−CT mixed-stack co-assembly leading to the molecularly dissolved A1 and emissive DPA molecules, as shown in Figure 1c. Further, the TIS−CT co-assembly was found to be thermally stable with melting temperature [$\alpha(T)$ = 0.5] of 339−343 K.

To gain further insights into the DPT and A1 molecular interactions responsible for the formation of supramolecular TIS−CT hydrogel, attenuated total reflection infrared (ATIR) and ^{1}H NMR experiments were performed (Figure 2f). Upon close inspection of the ATIR spectral regions 3732−2463 and 1765−1592 cm^{-1}, the intense, sharp amide N−H and carboxylic acid O−H signals of DPT (at 3320 and 3047 cm^{-1}, respectively) were found to be broadened in the TIS−CT xerogels. In addition, the carbonyl (C═O) stretching frequencies of A1 at 1748 cm^{-1} (ester C═O) and 1705 cm^{-1} (imide C═O) were shifted to lower frequency values (1741 and 1698 cm^{-1}, respectively) in TIS−CT xerogels. These spectral changes could be clearly attributed to the participation of the hydrogen-bonding interactions between the amide group in DPT and carbonyl groups (both ester and imide) of A1 to form extended 1D TIS−CT co-assembly; each of the 1D CT molecular stacks were further connected and assembled via hydrogen bonding involving carboxylic acid moieties on the backbone of DPT, thereby forming a network of dipoles, which is expected to have implications in the ferroelectric properties of the assembly.

To ascertain the role of water in TIS−CT hydrogel formation, we further carried out ^{1}H NMR titration experiments (Figure 2g). In comparison with the ^{1}H NMR spectra of DPT, A1, and DPT+A1 in DMSO-d_6 solution, their aqueous solutions showed significant upfield shifts and broadening of aromatic proton signals upon addition of different volumes of water (4−24 μL). For DPT, this was recorded as pyrene (8.29−7.96 and 8.18−7.91 ppm, $\Delta\delta_{DPT}$ = 0.11 ppm), while for A1 it was the NDI core (8.72−8.57 ppm, $\Delta\delta_{NDI}$ = 0.15 ppm). This was accompanied by the downfield shifting of amide NH protons (8.68−8.73 ppm, $\Delta\delta_{amide}$ = 0.05 ppm) of DPT. This

DOI: 10.1021/jacs.6b03811
J. Am. Chem. Soc. 2016, 138, 8259−8268

spectral shifting of aromatic and amide protons established hydrophobic force-induced intermolecular CT stacking of DPT and A1 stabilized by the intermolecular hydrogen bonding between amide protons of DPT and the imide carbonyl of A1, respectively. Under similar conditions, ^{1}H NMR titration experiments of individual DPT and A1 did not show appreciable spectral shifts in the pyrene (upfield shifts $\Delta\delta_{DPT}$ = 0.01 ppm) and NDI (downfield shifts $\Delta\delta_{NDI}$ = 0.006 ppm) core protons, respectively (Figures S9 and S10, SI). Therefore, the hydrogelation of the CT co-assembly of A1+DPT is a synergetic effect of complementary aromatic π-surface mixed-stacking interactions between DPT (pyrene, π-electron rich) and A1 (NDI core, π-electron deficient), supported by intermolecular hydrogen-bonding interactions within the TIS−CT co-assembly (between DPT amide NH protons and imide as well as ester CO of A1) and among the 1D TIS−CT molecular stacks (carboxylic acid functionalities on backbone of DPT), as shown in Figure 2h.[34,41]

The nanoscale morphology of the A1+DPT CT co-assembly structure in hydrogel was investigated by field emission scanning electron microscopy (FESEM) and atomic force microscopy (AFM) techniques. FESEM micrographs of A1 showed self-assembled 2D sheets with micrometer-long lateral dimensions (Figure S13, SI). However, under similar conditions, DPT failed to show any ordered self-assembled structures. Interestingly, the xerogels of A1+DPT (A1:DPT 2:1) CT co-assembly displayed an interconnected network of high aspect ratio 1D fibrils (Figure 3a). The AFM section analysis on these CT xerogels displayed hierarchical nanofiber bundles with an average topographical height of ∼4−16 nm and width of ∼60−150 nm (Figure 3b). The nature of molecular arrangement within 1D CT nanofibers of xerogel film was further probed by using powder X-ray diffraction (PXRD) measurements and compared with that of individual DPT and A1 films (Figure 3c). The film of A1 (2D sheets) displayed sharp diffraction peaks at 5.7° (15.4 Å) and 11.4° (7.7 Å), corresponding to molecular lateral dimensions, suggesting crystalline molecular packing within the 2D sheets. On the other hand, the pristine DPT sample did not exhibit significant diffraction signals, indicating its amorphous nature. Remarkably, the 1D CT nanofibrous xerogel film of A1+DPT displayed intense, sharp diffraction peaks at 5.7° (15.4 Å) and 11.4° (7.7 Å) along with the appearance of new diffraction peaks at 30.8° (2.9 Å) and 31.0° (2.8 Å), which correspond to hydrogen-bonding distances and reveal that the crystalline CT mixed-stacks are connected by intermolecular hydrogen-bonding interactions. The two diffraction signals for hydrogen-bonding interactions (2.9 and 2.8 Å) further support the TIS−CT co-assembly, held together by two distinct hydrogen-bonding interactions, i.e., intra- and inter-TIS−CT co-assembly, as shown in Figure 2h. Overall, it is clear that the formation of 1D crystalline nanofibers of A1+DPT is the result of efficient synergy between intermolecular CT and hydrogen-bonding interactions to form extended (D−A−D−A) co-assembly structures.

Moreover, the TIS−CT co-assembly was found to be light-responsive; the UV-irradiated (λ = 365 nm) CT solution turned black in color and exhibited a new set of absorption bands at 502, 612, and 750 nm. The solution reverted its original state gradually within 80 min in dark conditions (Figure 4a). The signature absorption characteristics upon UV exposure match with that of the NDI radical anion and were ascribed to the doublet D_0 to D_n transitions.[42−44] Interestingly, the plot of

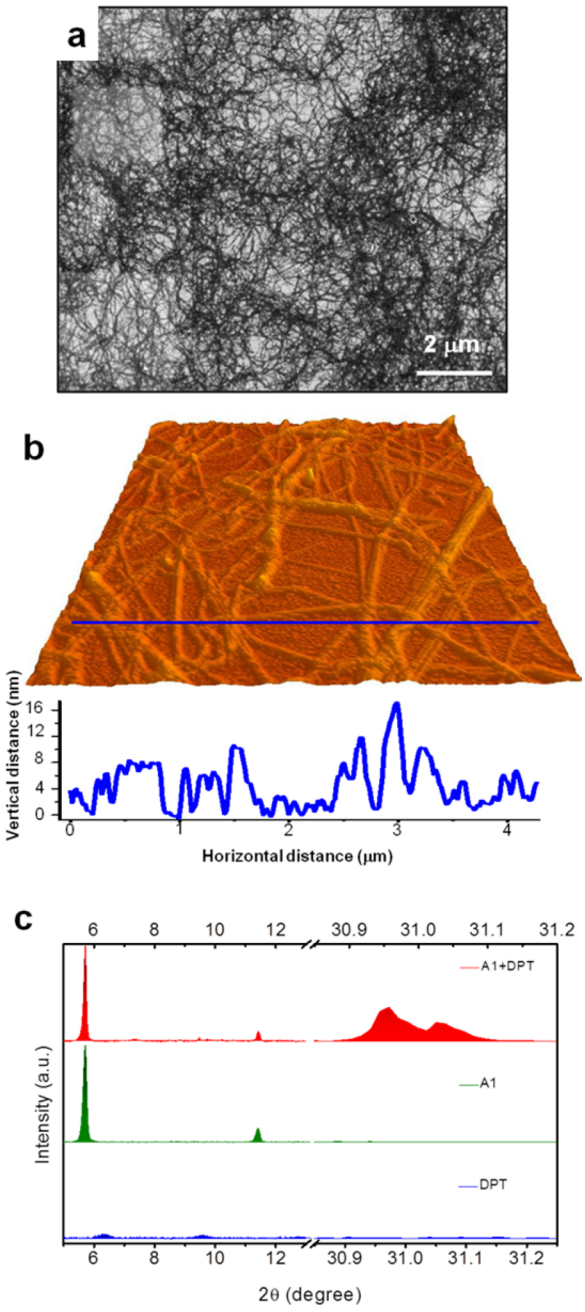

Figure 3. Morphological and structural analysis of A1+DPT CT-TIS xerogel. (a) FESEM image showing high aspect ratio fibrils. (b) AFM 3D-image and section analysis (along the blue line) of nanofibrils. (c) Thin-film PXRD pattern (5°−13° and 30.8°−31.3°) of A1, DPT, and TIS−CT xerogel.

absorbance at 750 nm versus the number of cycles of UV-irradiation and in the dark clearly showed the reversible photoinduced single-electron transfer (PISET) switching within the TIS−CT co-assembly, and this was found to be effective even after six cycles, as shown in Figure 4b.

Further, we utilize the color tunability of the co-assembly as a prospective optical memory element (discussed in the later sections). This PISET-reaction-driven formation of $A1^{\bullet-}$ was further confirmed by ^{1}H NMR experiments conducted with and without UV-irradiated A1+DPT CT solution. The UV-irradiated ^{1}H NMR spectra displayed complete disappearance of a signal (δ = 8.57 ppm) corresponding to NDI core protons

DOI: 10.1021/jacs.6b03811
J. Am. Chem. Soc. 2016, 138, 8259−8268

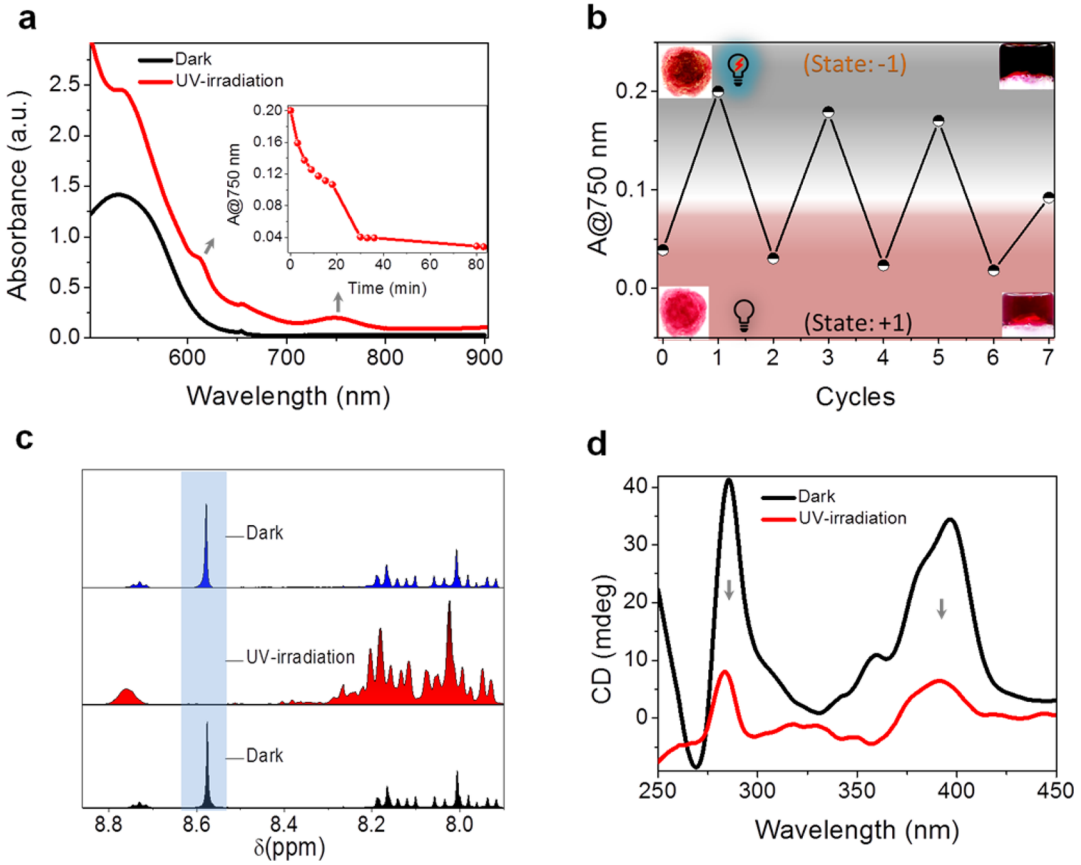

Figure 4. UV-irradiation ($h\nu$ 365 nm)-responsive photoinduced single-electron transformation reaction within the A1+DPT chiral TIS−CT co-assembly. (a) UV−vis−NIR spectra of TIS−CT co-assembly in the dark and upon UV-irradiation. Inset: Plot of absorbance at 750 nm versus time (minutes) after UV-irradiation. (b) Switching cycles exhibiting optical memory. Inset: Respective color changes in the TIS−CT hydrogel and thin film. (c) ^{1}H NMR spectra of TIS−CT co-assembly in the dark and upon UV-irradiation. (d) CD spectra of TIS−CT co-assembly in the dark and upon UV-irradiation.

of A1, signifying the formation of $NDI^{\bullet-}$ (Figure 4c).[42] However, keeping this UV-irradiated A1+DPT CT solution under dark conditions for 3 h resulted in the reappearance of the signal for NDI core protons (δ = 8.57 ppm) of A1. Therefore, the ^{1}H NMR study convincingly revealed the reversibility of the PISET reaction within the TIS−CT co-assembly. Furthermore, the PISET within the chiral TIS−CT co-assembly resulted in decreased ICD signals, owing to the $A1^{\bullet-}$ radical-induced breaking of heterochromophoric exciton coupling between DPT (pyrene) and A1 (NDI), respectively (Figure 4d). Interestingly, upon keeping the sample under dark condition for 80 min, the ICD signals were restored. Thus, it can be concluded that the chiral donor (DPT) and acceptor (A1/A2) intermolecular orientation within the mixed-stack CT co-assembly can be modulated by external stimuli, such as light. Similarly, the phenomenon of UV-induced color changes was also observed in thin-film form and hydrogels [Figures 4b and S15 (SI)].

As a next step, we develop a thin-film capacitive device structure from solution-processable co-assembled TIS−CT structures and highlight the ferroelectric nature of the system. The device fabrication for C−V measurements involved introducing the CT mixture, i.e., A1+DPT xerogel film (thickness 0.7−1 μm with rms roughness <10%) onto the bottom ITO/Au electrodes followed by drying the gel under a vacuum of 10^{-3} mbar to obtain a uniform film. Au top electrode was then coated on the top to complete the devices (inset in Figure 5d), which exhibited low-leakage currents. Capacitance and polarization measurements [$P(E)$] were studied over a temperature range of 100−300 K and frequency range from 100 Hz to 10 MHz (Figure 5) to estimate the magnitude of spontaneous polarization and observe the crossover to the paraelectric state. Typical ferroelectric loops with a larger presence of spontaneous polarization at the low temperature of 100 K (Figure 5a) was observed. More importantly, this ferroelectric polarization loop persisted even at room temperature and beyond. Saturation polarization (P_{sat}) at 300 K was observed to be ~4 $\mu C/cm^2$, as shown in Figure 5b, which increased to 6 $\mu C/cm^2$ at 100 K. Significant increase in the area under polarization was observed at low temperature. This observed increase in the area of the $P-E$ loop is attributed to the freezing of the various dielectric loss mechanisms.[45,46] Similarly, at frequencies larger than 10 kHz, the capacitors demonstrated lossy behavior due to stray conductance originating from leakage currents. Nevertheless, the demonstration of the ferroelectric polarization loop shown in Figure 5b in a simple capacitive structure could be interpreted as a simplistic first-generation nonvolatile random access electric memory with two polarization states corresponding to $+P_{sat}$ (state +1) and $-P_{sat}$ (state −1).

To further understand the nature of the ferroelectricity, dielectric constant (ε_r) measurement was performed over a temperature (T) range of 100−360 K. The typical trend of $\varepsilon_r(T)$ is shown in Figure 5d. As evident from the data, $\varepsilon_r(T)$

DOI: 10.1021/jacs.6b03811
J. Am. Chem. Soc. 2016, 138, 8259−8268

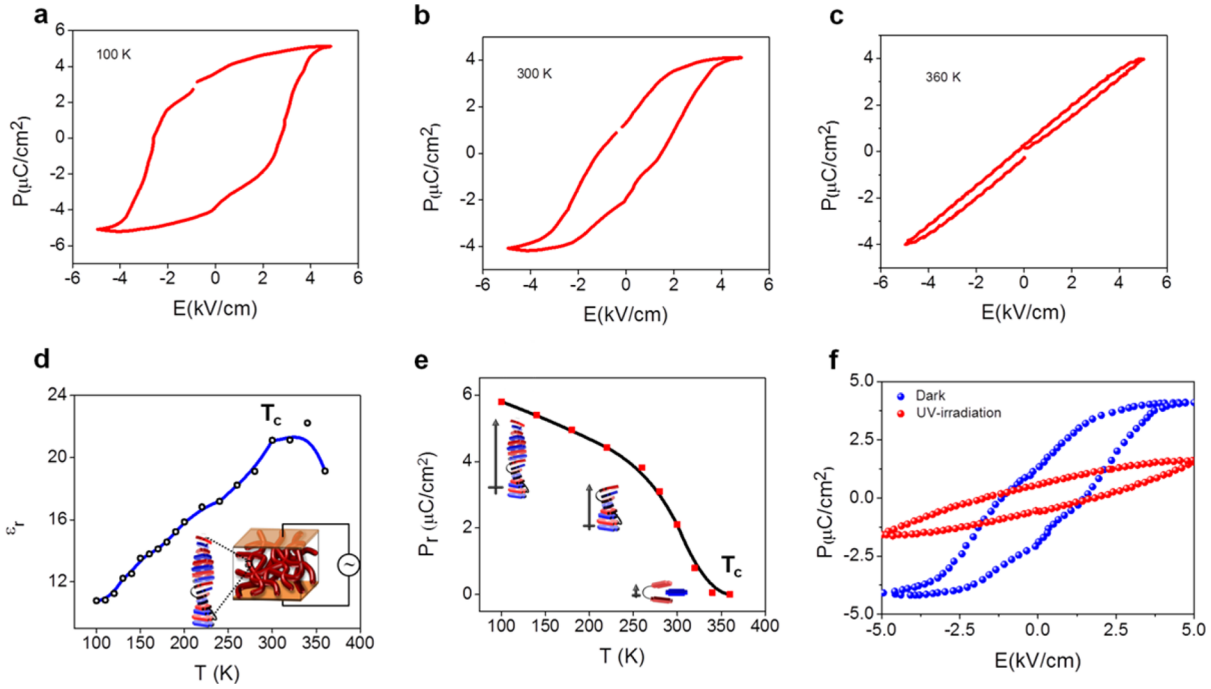

Figure 5. Ferroelectric measurements on A1+DPT chiral TIS−CT co-assembled xerogel thin-films. *P*−*E* Loop measurements at different temperatures: (a) 100 K, (b) 300 K, and (c) 360 K. (d) Bulk dielectric constant measured as a function of temperature showing a clear phase transition. Inset: The typical device schematic utilized for the dielectric measurement. (e) Variation of the spontaneous polarization as a function of temperature. Inset: The schematic dipolar alignment with *T*. (f) Photoresponsive ferroelectric switching device.

exhibits a monotonic increase with respect to *T*. In the regime $T > 340$ K, the phase transition signature in $\varepsilon_r(T)$ is observed. The modeling of $\varepsilon_r(T)$ to a standard Curie−Weiss law indicates an order−disorder-type phase transition.[10,47] A clear phase transition is also indicated by the characteristics of the remnant polarization with temperature (Figure 5e). The dipole moment in the ferroelectric phase (P_s/N, where *N* is the dipole density) was estimated to be $\sim 2 \times 10^{-29}$ C m at 300 K.

Observation of ferroelectricity in materials requires the existence of a long-range interaction, which results in a finite polarization in the absence of an external field. The presence of a macroscopic axis representing the polarization in the ferroelectric state was also evident in optical anisotropy measurements of the films. A liquid crystal (LC) modulator was utilized in this setup for transmitting (wavelength 536 nm suitable for ferroelectric film absorption window), and an electronic controller was used to rotate the polarization in defined steps. The polarization axis of LC was rotated continuously at a given rate while a static position was maintained and the signal was digitally monitored, and the transmission profiles clearly indicated anisotropy. This feature of anisotropy was considerably reduced upon UV-exposure.

In the case of A1+DPT, the presence of chirality and CT interaction, as well as hydrogen-bonding interaction, provides the prerequisite for the finite dipolar character to the supramolecular assembly. The long-range order is then governed by the interfibrillar hydrogen-bonding interactions, as evident from the IR spectra shown in Figure 2f. To confirm that these interactions were driving the long-range polarization, thermal and optical probing of the assembly was performed along with simultaneous measurement of the polarization property. Upon UV-illumination (λ = 365 nm), the saturation characteristic observed in the *P*−*E* loop was removed. Illumination increased the leakage current in the sample and the *P*−*E* loop was converted to that of a lossy capacitor (Figure 5f). The observed loss of ferroelectricity upon illumination can be correlated with the formation of radical anions of the respective species A1 (as seen in the absorption spectra, Figure 4a) and the loss of chirality, which gets reflected in the polarization of the system. Temperature-dependent dielectric measurement and loss of ferroelectricity by photoirradiation are linked to the origin of ferroelectricity. Ordered supramolecular 3-D interconnected structures supported by the combination of chiral CT and hydrogen-bonding interactions are expected to be responsible for the observed ferroelectricity property in these thin films. Moreover, the observation of color and polarization tunability of the CT co-assembly in a thin-film architecture allows the possibility to design a smart optoelectronic memory with optical control of electronic polarization along with the visible color change representative of a two-state memory. We define the CT state as the +1 state, and the process of UV-illumination can be referred as an erasing process that drives the TIS−CT co-assembly to the radical anion/unpolarized state (Figure 1c) referred to as the −1 state. A schematic showing the various states of the optoelectronic memory is shown in Figure 4b and Movie 2.

The simplicity of the fabrication of TIS−CT co-assembly of A1+DPT was demonstrated in the solid state and on a flexible substrate [Figures 1b and S14 (SI)]. The binary mixture of DPT and A1 (1:2) was subjected to cogrinding using mortar and pestle in the absence of any solvent. A red, nonfluorescent TIS−CT co-assembly developed almost instantly from the originally colorless and highly fluorescent DPT and A1 solid powders (Figure 1b). On the other hand, we used invisible DPT solution (UV-ink, blue under UV light) as the ink to write "U" on a flexible filter paper and A1 solution as the spray for visible (naked eye) readout; a red CT complex formed in the written area (Figure S14, SI). Such a simple mechanical and

DOI: 10.1021/jacs.6b03811
J. Am. Chem. Soc. 2016, 138, 8259−8268

solution processing method to form patterns of A1+DPT co-assembly has wide implications in fabricating inexpensive, large-scale, flexible-patterned pressure sensors and has electronic memory device applications.

CONCLUSIONS

In conclusion, we designed and demonstrated a new class of π-conjugated donor−acceptor molecular systems and their multi-stimuli-responsive extended supramolecular chiral mixed-stack TIS−CT hydrogels with nanofibrous 3D networks as a promising room-temperature thin-film organic ferroelectric material. A variety of spectroscopic techniques were utilized to probe the dynamics of the assembly and to understand the origin of polarization in the CT co-assembly. The described supramolecular engineering was based on the synergy between CT and hydrogen-bonding interactions to generate interconnected 1D TIS−CT stacks, wherein donor (DPT)−acceptor (A1) dimerization broke the center of symmetry of the lattice and the corresponding supramolecular chirality, leading to spontaneous unidirectional alignment of the net molecular dipoles. The nanofibrous network of A1+DPT TIS−CT co-assembly was utilized to fabricate a solution-processable supramolecular thin-film ferroelectric capacitor with $P_s \sim 4$ $\mu C/cm^2$ at room temperature. Moreover, the PISET reaction within the TIS−CT co-assembly provided photoresponsivity to the assembly and enabled the design of optical and electronically rewritable multistate memory. This novel design strategy to fabricate multi-stimuli-responsive, room-temperature ferroelectric memory is expected to catalyze the design and development of future large-area solution-processable multicomponent supramolecular systems for smart functional organics.

EXPERIMENTAL SECTION

Materials. Ethylenediaminetetraacetic dianhydride (EDTA dianhydride), 1-pyrenemethylamine hydrochloride, 1,4,5,8-naphthalenetetracarboxylic acid dianhydride (NDA), *N,N*-diisopropylethylamine, 1-hydroxybenzotriazole, L-alanine, and D-alanine were obtained from Sigma-Aldrich. All other reagents and solvents were of reagent grade and used without further purification.

Synthetic Procedure and Characterization. *Synthesis of Dipyrene Tweezer (DPT).* EDTA dianhydride (0.5 mg, 1.9 mmol) and pyrenemethylamine hydrochloride (1g, 4 mmol) were dispersed into 20 mL of *N,N*-dimethylformamide. After 15 min, triethylamine (0.5 mL, 4.2 mmol) was added dropwise, and the mixture was allowed to stir overnight at room temperature. The resulting precipitate was filtered and washed with ice-cold water to afford a white solid in quantitative yield.

Characterization Data for DPT. Yield 82%; ^{1}H NMR (DMSO-d_6, 400 MHz) δ_H 12.28 (2H, s), 8.70 (2H, t), 8.29−7.96 (18H, m), 4.97 (4H, d), 3.36 (8H, d), 2.78 (4H, s); ^{13}C NMR (DMSO-d_6, 400 MHz) δ_C 172.5, 170.5, 132.3, 130.7, 130.2, 129.9, 127.8, 127.4, 127.3, 126.8, 126.1, 125.1, 124.6, 123.9, 123.8, 122.9, 57.4, 55.1, 52.3, 40.1; HRMS m/z $[M + H]^+$ calcd for $C_{44}H_{39}N_4O_6$ 719.2864, found 719.2821.

Synthesis of Amino Acid Methyl Ester. Anhydrous methanol (50 mL) was placed into a 100 mL two-necked round-bottom flask, fitted with a reflux condenser and an additional dropping funnel, and cooled to ice temperature. Acetyl chloride (3 mL) was added dropwise through the dropping funnel. After 15 min, alanine (6.9 g, 18.16 mmol) was added and the reaction mixture was refluxed overnight at 70 °C. The reaction mixture was dried in vacuo to obtain alanine methyl ester hydrochloride in quantitative yield, which was used for further reaction without purification.

Synthesis of A1 and A2. 1,4,5,8-Naphthalenetetracarboxylic dianhydride (0.5 g, 1.8 mmol) and α-(L/D)-alanine methyl ester (0.52 g, 3.72 mmol) were suspended in 10 mL of dimethylformamide (DMF). To this suspension was added triethylamine (TEA) (0.2 mL) and the mixture was allowed to reflux for 12 h. After cooling to room temperature, the solvent was removed and added into 250 mL of distilled water. The precipitate was collected through a suction funnel and washed with an excess of distilled water. The organic layer was separated and dried under vacuo, and the residue was purified by column chromatography (CH_2Cl_2/MeOH 10/1).

Characterization Data for A1. Yield 82%; ^{1}H NMR (DMSO-d_6, 400 MHz) δ_H 8.72 (4H, s), 5.72 (2H, q), 3.64 (6H, s), 1.58 (6H, d); ^{13}C NMR (DMSO-d_6, 100 MHz) δ_C 170.0, 162.0, 131.0, 126.3, 126.1, 52.2, 48.9, 14.2; HRMS (ESI) m/z $[M + H]^+$ calcd for $C_{22}H_{19}N_2O_8$ 439.1136, found 439.1144.

Characterization Data for A2. Yield 78%; ^{1}H NMR (DMSO-d_6, 400 MHz) δ_H 8.72 (4H, s), 5.72 (2H, q), 3.64 (6H, s), 1.58 (6H, d); ^{13}C NMR (DMSO-d_6, 100 MHz) δ_C 170.0, 162.0, 131.0, 126.3, 126.1, 52.2, 48.9, 14.2; HRMS (ESI) m/z $[M + H]^+$ calcd for $C_{22}H_{19}N_2O_8$ 439.1136, found 439.1145.

Absorption Spectroscopy. UV−vis spectra were recorded on a PerkinElmer model Lambda 900 spectrophotometer. Titration experiment was performed by adding different ratios of A1/A2 to a fixed concentration of DPT (200 μM) in aqueous solution (DMSO/water 20/80), and the samples were analyzed in a quartz cuvette of 10 mm path length.

Fluorescence Spectroscopy. Fluorescence spectra were recorded on a PerkinElmer model LS 55 spectrophotometer. All fluorescence emission spectra in solution and in the solid state were recorded with excitation wavelength λ_{ex} = 340 nm except for A1/A2 alone (λ_{ex} = 380 nm). The titration experiment was performed by adding different ratios of A1/A2 to a fixed concentration of DPT (200 μM) in aqueous solution (DMSO/water 20/80), and the samples were analyzed in a quartz cuvette of 10 mm path length. For solid-state optical measurements, samples were prepared by mechanical cogrinding of a 1:2 mixture of DPT (5 mg, 6.9 mmol) and acceptor (A1/A2, 5.3 mg, 13.9 mmol), using a mortar and pestle, into a fine brick-red-colored solid powder. Spectra of resultant solid powders were recorded in front face geometry with 340 nm excitation wavelength.

NMR Spectroscopy. ^{1}H and ^{13}C NMR spectra were recorded on a Bruker AV-400 spectrometer with chemical shifts reported as ppm (in DMSO-d_6/$CDCl_3$ with tetramethylsilane as internal standard). Solvent-dependent ^{1}H NMR studies were performed by adding different volumes of deionized water (5, 10, 15, 20, 25, and 30 μL) to the well-mixed solution of DPT:A1/A2 (1:2) in DMSO-d_6 (400 μL).

ATIR Spectroscopy. ATIR spectra were recorded on a Bruker IFS 66/V spectrometer. The measurements were done on aqueous solutions of solid powders of A1 and DPT and xerogels of A1+DPT that were highly vacuum dried at room temperature.

Mass Spectrometry (MS). High-resolution mass spectra (HRMS) were obtained from on Agilent Technologies 6538 UHD Accurate-Mass Q-TOF LC/MS spectrometer.

Field-Emission Scanning Electron Microscopy (FESEM). FESEM images were acquired with a FEI Nova nanoSEM-600 equipped with a field-emission gun operating at 15 kV. The samples were prepared by transfer of aqueous solutions of A1, DPT, and A1+DPT CT hydrogels onto a Si(111) substrate and drying in air followed by vacuum drying at room temperature.

Atomic Force Microscopy (AFM). AFM images were acquired under ambient conditions using an Innova (Veeco) atomic force microscope in dynamic force (tapping) mode. The samples were prepared as A1+DPT CT hydrogels applied onto Si(111) and allowed to dry in air followed by vacuum drying at room temperature. AFM section analysis was done offline.

Powder X-ray Diffraction (PXRD). PXRD patterns were recorded on xerogels of A1+DPT CT with a Rigaku-99 (Miniflex) diffractometer using Cu Kα radiation (λ = 1.5406 Å). The xerogels were prepared by applying CT hydrogel onto an ultraclean glass slide and allowed to dry in air followed by vacuum drying at room temperature. The diffraction peaks were indexed by the DICVOL program.

Gelation Experiments. DPT (25 μL) and 50 μL of A1/A2 (from the stock solutions of DPT and A1/A2 i.e., 8 mM in DMSO) were

DOI: 10.1021/jacs.6b03811
J. Am. Chem. Soc. 2016, 138, 8259−8268

mixed together in 25 μL of DMSO. The mixture was gently heated for 5 min and then 400 μL of deionized water was slowly added under ultrasonication. The resultant aqueous solution spontaneously transformed into a red, nonfluorescent hydrogel. The gel formation is determined by tilting/inverting the sample vial upside down.

Ferroelectric and Dielectric Measurements. For the polarization measurement of the supramolecular assembly, the typical sandwich device structure ITO/Au/CT assembly/Au as shown in the inset of Figure 5d was fabricated. ITO electrodes were obtained from Xinyan Technology Ltd. (15 ohm/∼) and patterned into 1 mm × 15 mm electrodes. A thin layer of Au electrode (∼20 nm) was coated on patterned ITO substrates at 10^{-6} mbar and a rate of 1 Å/s. Xerogels of the assembly were introduced on top of Au-coated ITO electrodes. This was followed by the evaporation of another Au layer (10^{-6} mbar, 1 Å/s, and 40 nm thick). Dielectric constant measurements were performed in the standard C−V set up of a SCS 4200 semiconductor parameter analyzer. Polarization measurement was performed using a combination of a standard physical property measurement system from Quantum Design Inc. and a high voltage source from Radiant Technology Precision Workstation. For the temperature-dependence measurement, the samples were maintained at a high vacuum of 10^{-4}−10^{-5} mbar, and the temperature was varied using a closed cycle cryo setup from Cryogenics Technology Inc.

■ ASSOCIATED CONTENT

Supporting Information

The Supporting Information is available free of charge on the ACS Publications website at DOI: 10.1021/jacs.6b03811.

Additional spectral studies (Figures S1−S15) (PDF)
Movie 1 (AVI)
Movie 2 (AVI)

■ AUTHOR INFORMATION

Corresponding Authors

*narayan@jncasr.ac.in
*tgraju@jncasr.ac.in

Notes

The authors declare no competing financial interests.

■ ACKNOWLEDGMENTS

Authors thank Prof. C. N. R. Rao FRS for constant support and encouragement, JNCASR, Department of Biotechnology (DBT) (IYBA grant BT/03/IYBA/2010 and Special Nanotechnology Task Force grant: BT/PR10263/NNT/28/711/2013), and Department of Science and Technology, India for financial support, S.P.S. thanks CSIR, India, for fellowship.

■ REFERENCES

(1) Aida, T.; Meijer, E. W.; Stupp, S. I. *Science* **2012**, *335*, 813−817.
(2) Collet, E.; Lemee-Cailleau, M. H.; Buron-Le Cointe, M.; Cailleau, H.; Wulff, M.; Luty, T.; Koshihara, S. Y.; Meyer, M.; Toupet, L.; Rabiller, P.; Techert, S. *Science* **2003**, *300*, 612−615.
(3) Faramarzi, V.; Niess, F.; Moulin, E.; Maaloum, M.; Dayen, J.-F.; Beaufrand, J.-B.; Zanettini, S.; Doudin, B.; Giuseppone, N. *Nat. Chem.* **2012**, *4*, 485−490.
(4) Aliprandi, A.; Mauro, M.; De Cola, L. *Nat. Chem.* **2016**, *8*, 10−15.
(5) Daeneke, T.; Kwon, T.-H.; Holmes, A. B.; Duffy, N. W.; Bach, U.; Spiccia, L. *Nat. Chem.* **2011**, *3*, 211−215.
(6) Facchetti, A.; Annoni, E.; Beverina, L.; Morone, M.; Zhu, P.; Marks, T. J.; Pagani, G. A. *Nat. Mater.* **2004**, *3*, 910−917.
(7) Sirringhaus, H.; Brown, P. J.; Friend, R. H.; Nielsen, M. M.; Bechgaard, K.; Langeveld-Voss, B. M. W.; Spiering, A. J. H.; Janssen, R. A. J.; Meijer, E. W.; Herwig, P.; de Leeuw, D. M. *Nature* **1999**, *401*, 685−688.
(8) Sirringhaus, H.; Tessler, N.; Friend, R. H. *Science* **1998**, *280*, 1741−1744.
(9) Zhuang, J.; Gordon, M. R.; Ventura, J.; Li, L.; Thayumanavan, S. *Chem. Soc. Rev.* **2013**, *42*, 7421−7435.
(10) Horiuchi, S.; Tokura, Y. *Nat. Mater.* **2008**, *7*, 357−366.
(11) Tayi, A. S.; Kaeser, A.; Matsumoto, M.; Aida, T.; Stupp, S. I. *Nat. Chem.* **2015**, *7*, 281−294.
(12) Scott, J. F. *Science* **2007**, *315*, 954−959.
(13) Li, J.; Liu, Y.; Zhang, Y.; Cai, H. L.; Xiong, R. G. *Phys. Chem. Chem. Phys.* **2013**, *15*, 20786−20796.
(14) Miyajima, D.; Araoka, F.; Takezoe, H.; Kim, J.; Kato, K.; Takata, M.; Aida, T. *Science* **2012**, *336*, 209−213.
(15) Lovinger, A. J. *Science* **1983**, *220*, 1115−1121.
(16) Solomon, A. L. *Phys. Rev.* **1956**, *104*, 1191−1191.
(17) Bordeaux, D.; Bornarel, J.; Capiomont, A.; Lajzerowicz-Bonneteau, J.; Lajzerowicz, J.; Legrand, J. F. *Phys. Rev. Lett.* **1973**, *31*, 314−317.
(18) Fu, D. W.; Cai, H. L.; Liu, Y.; Ye, Q.; Zhang, W.; Zhang, Y.; Chen, X. Y.; Giovannetti, G.; Capone, M.; Li, J.; Xiong, R. G. *Science* **2013**, *339*, 425−428.
(19) Tayi, A. S.; Shveyd, A. K.; Sue, A. C.; Szarko, J. M.; Rolczynski, B. S.; Cao, D.; Kennedy, T. J.; Sarjeant, A. A.; Stern, C. L.; Paxton, W. F.; Wu, W.; Dey, S. K.; Fahrenbach, A. C.; Guest, J. R.; Mohseni, H.; Chen, L. X.; Wang, K. L.; Stoddart, J. F.; Stupp, S. I. *Nature* **2012**, *488*, 485−489.
(20) Zhang, W.; Xiong, R. G. *Chem. Rev.* **2012**, *112*, 1163−1195.
(21) Horiuchi, S.; Kumai, R.; Tokura, Y. *Chem. Commun.* **2007**, 2321−2329.
(22) Horiuchi, S.; Kobayashi, K.; Kumai, R.; Minami, N.; Kagawa, F.; Tokura, Y. *Nat. Commun.* **2015**, *6*, 7469−7475.
(23) Kagawa, F.; Horiuchi, S.; Matsui, H.; Kumai, R.; Onose, Y.; Hasegawa, T.; Tokura, Y. *Phys. Rev. Lett.* **2010**, *104*, 227602.
(24) Kobayashi, K.; Horiuchi, S.; Kumai, R.; Kagawa, F.; Murakami, Y.; Tokura, Y. *Phys. Rev. Lett.* **2012**, *108*, 237601.
(25) Blackburn, A. K.; Sue, A. C.; Shveyd, A. K.; Cao, D.; Tayi, A.; Narayanan, A.; Rolczynski, B. S.; Szarko, J. M.; Bozdemir, O. A.; Wakabayashi, R.; Lehrman, J. A.; Kahr, B.; Chen, L. X.; Nassar, M. S.; Stupp, S. I.; Stoddart, J. F. *J. Am. Chem. Soc.* **2014**, *136*, 17224−17235.
(26) Okamoto, H.; Mitani, T.; Tokura, Y.; Koshihara, S.; Komatsu, T.; Iwasa, Y.; Koda, T.; Saito, G. *Phys. Rev. B: Condens. Matter Mater. Phys.* **1991**, *43*, 8224−8232.
(27) Lemieux, R. P. *Acc. Chem. Res.* **2001**, *34*, 845−853.
(28) Popova, E. V.; Fedoryako, A. P.; Drushlyak, T. G.; Vashchenko, V. V.; Kutulya, L. A. *Ferroelectrics* **2006**, *343*, 33−40.
(29) Boulton, C. J.; Finden, J. G.; Yuh, E.; Sutherland, J. J.; Wand, M. D.; Wu, G.; Lemieux, R. P. *J. Am. Chem. Soc.* **2005**, *127*, 13656−13665.
(30) Hirst, A. R.; Escuder, B.; Miravet, J. F.; Smith, D. K. *Angew. Chem., Int. Ed.* **2008**, *47*, 8002−8018.
(31) Moulin, E.; Cid, J. J.; Giuseppone, N. *Adv. Mater.* **2013**, *25*, 477−487.
(32) Safont-Sempere, M. M.; Fernandez, G.; Wurthner, F. *Chem. Rev.* **2011**, *111*, 5784−5814.
(33) Hardouin-Lerouge, M.; Hudhomme, P.; Salle, M. *Chem. Soc. Rev.* **2011**, *40*, 30−43.
(34) Zhu, Z.; Cardin, C. J.; Gan, Y.; Colquhoun, H. M. *Nat. Chem.* **2010**, *2*, 653−660.
(35) Pandeeswar, M.; Khare, H.; Ramakumar, S.; Govindaraju, T. *Chem. Commun.* **2015**, *51*, 8315−8318.
(36) Avinash, M. B.; Govindaraju, T. *Adv. Mater.* **2012**, *24*, 3905−3922.
(37) Pandeeswar, M.; Khare, H.; Ramakumar, S.; Govindaraju, T. *RSC Adv.* **2014**, *4*, 20154−20163.
(38) Bhosale, S.; Sisson, A. L.; Talukdar, P.; Furstenberg, A.; Banerji, N.; Vauthey, E.; Bollot, G.; Mareda, J.; Roger, C.; Wurthner, F.; Sakai, N.; Matile, S. *Science* **2006**, *313*, 84−86.
(39) Ghosh, S.; Ramakrishnan, S. *Angew. Chem., Int. Ed.* **2004**, *43*, 3264−3268.
(40) Scott Lokey, R.; Iverson, B. L. *Nature* **1995**, *375*, 303−305.
(41) Koshkakaryan, G.; Klivansky, L. M.; Cao, D.; Snauko, M.; Teat, S. J.; Struppe, J. O.; Liu, Y. *J. Am. Chem. Soc.* **2009**, *131*, 2078−2079.
(42) Guha, S.; Saha, S. *J. Am. Chem. Soc.* **2010**, *132*, 17674−17677.

DOI: 10.1021/jacs.6b03811
J. Am. Chem. Soc. 2016, 138, 8259−8268

(43) Song, Q.; Li, F.; Wang, Z.; Zhang, X. *Chem. Sci.* **2015**, *6*, 3342−3346.
(44) Kumar, S.; Ajayakumar, M. R.; Hundal, G.; Mukhopadhyay, P. *J. Am. Chem. Soc.* **2014**, *136*, 12004−12010.
(45) Senanayak, S. P.; Guha, S.; Narayan, K. S. *Phys. Rev. B: Condens. Matter Mater. Phys.* **2012**, *85*, 115311.
(46) Senanayak, S. P.; Narayan, K. S. *Adv. Funct. Mater.* **2014**, *24*, 3324−3331.
(47) Horiuchi, S.; Tokunaga, Y.; Giovannetti, G.; Picozzi, S.; Itoh, H.; Shimano, R.; Kumai, R.; Tokura, Y. *Nature* **2010**, *463*, 789−792.

DOI: 10.1021/jacs.6b03811
J. Am. Chem. Soc. 2016, 138, 8259−8268